photonics

MDPI

Article

Design of a Measuring Device and Experimental Study into the Relationship between Temperature and the Density of Alkali Metal-Vapor

Huining Shang [1], Sheng Zou [1,2,*], Wei Quan [1,2,*], Binquan Zhou [1,2], Shun Li [1,2], Weiyong Zhou [2] and Fengwen Zhao [1]

[1] School of Instrumentation and Optoelectronic Engineering, Beihang University, Beijing 100191, China
[2] Hangzhou Innovation Institute, Beihang University, Hangzhou 310051, China
* Correspondence: zousheng@buaa.edu.cn (S.Z.); quanwei@buaa.edu.cn (W.Q.)

Abstract: The temperature of the alkali metal cell, which affects the density of the alkali-metal vapor and the gas pressure, is usually difficult to measure directly. However, the temperature of the alkali-metal cell and the density of the alkali-metal vapor are important parameters that affect the performance of the atomic sensor. In this paper, a device that can directly measure the internal temperature of an alkali metal cell in real time is designed for the first time to explore the relationship between alkali-metal vapor density and temperature. Alkali-metal vapor density is measured using the absorption spectrum. The pressure broadening model, combined with the transition of four hyperfine levels, was used to fit the absorption line of ^{87}Rb D1 under the action of 700 Torr N_2, and a good fitting effect was obtained. The experimental results show that the density of ^{87}Rb is less than the value calculated by the empirical formula. Based on the experimental results, we give the calculation formula of ^{87}Rb density with an uncertainty of only 4% and obtain the temperature dependence index of the line width and linear displacement of ^{87}Rb in N_2 by analyzing the absorption spectrum.

Keywords: absorption spectrum; alkali metal cell temperature; alkali-metal vapor density

Citation: Shang, H.; Zou, S.; Quan, W.; Zhou, B.; Li, S.; Zhou, W.; Zhao, F. Design of a Measuring Device and Experimental Study into the Relationship between Temperature and the Density of Alkali Metal-Vapor. *Photonics* **2023**, *10*, 112. https://doi.org/10.3390/photonics10020112

Received: 2 December 2022
Revised: 5 January 2023
Accepted: 17 January 2023
Published: 21 January 2023

1. Introduction

The alkali-metal vapor density in the cell is of great significance for the study of atomic sensors, such as atomic magnetometers and atomic gyroscopes. In atomic magnetometers, the alkali metal cell contains alkali metal (one or more of K, Rb, and CS) and gas (one or more of helium, nitrogen, and inert gas) [1–3]. The parameters related to the sensitivity of the magnetometer, such as optical depth, atomic polarization, atomic relaxation rate, etc., are affected by the alkali metal vapor density. The alkali vapor density also has an important effect on the performance of the atomic gyroscopes. Noble-gas atoms with nonzero nuclear spin, such as ^{3}He, ^{21}Ne, ^{83}Kr, ^{129}Xe, and so on, collide with spin-polarized atoms of alkali metal via spin-exchange optical pumping to acquire polarization [4]. Due to the relatively long spin-lattice time, spin-polarized nuclei offer excellent performance in terms of stability and sensitivity, so they are widely used in precision measurement [5]. Recently, efficiently yielding large quantities of spin-polarized nuclei has become a compelling field of research [6–8]. In the case of noble-gas nuclei, the alkali vapor density affecting the spin-exchange rate limits the achievable level and the rate of hyperpolarization.

By referring to T. J. Killian's research on the saturated vapor pressure of alkali metal, the number density of alkali-metal vapor can be acquired from the ideal gas law [9]. Based on this finding, Alcock et al. [10] supplemented the saturated vapor pressure formula of alkali-metal vapor. Afterward, the formula has been widely used to calculate the pressure and density of alkali-metal vapor [8,11–14]. However, with respect to the situation of alkali-metal vapor inside a sealed glass cell, the observed vapor density deviates from

the empirical formula by as much as a factor of two [15]. There are some hypotheses to explain it, but the reason is still incompletely understood [16–19]. Due to the fact that the alkali metal is encapsulated inside the cell, the temperature inside the cell is hard to detect directly. Conventionally, a temperature sensor is attached to the surface of the cell [20–22]. There is a potential temperature difference between the inside and outside of the cell, which could be one source of error [23].

The motivation behind this paper is to avoid the error rooted in the temperature difference between the inside and outside of the cell, thereby offering a foundation for determining the actual alkali vapor density accurately by comparing the saturated-vapor-density curves. First, a collision-broadening line shape has been employed to evaluate rubidium-87 vapor density (see details in Section 2). Then, we designed a temperature measurement device by sealing an RTD inside the cell, which provides the feasibility for measuring internal temperature. The relevant spectral absorption equipment fitting the above device has been set up (see details in Section 3). The corresponding experimental results are discussed in Section 4.

2. Basic Principles

2.1. Relationship between Alkali-Metal Vapor Density and Temperature

The empirical formula of the vapor pressure for the alkali metal recommended by Alcock et al. [10] is as follows:

$$\log p_{atm} = A + \frac{B}{T}, \tag{1}$$

where T is the temperature of the alkali vapor in units of K, p_{atm} is the saturated vapor pressure of the alkali metal vapor in units of atm, and A and B are the parameters that depend on the type and phase of the alkali metals. For liquid Rb, A is 4.312, and B is -4040 [10].

According to the ideal gas law, the relationship between the vapor density and the vapor pressure of alkali metals can be expressed as:

$$p_{Pa} = Nk_BT, \tag{2}$$

where p_{Pa} is the saturated vapor pressure of the alkali metal vapor in units of Pa, N is the number density of alkali metals in units of m^{-3}, and k_B is the Boltzmann constant.

When we convert the unit of pressure in Equations (1) and (2) to Torr, the result is as follows:

$$\log p_{Torr} = 2.881 + A + \frac{B}{T}, \tag{3}$$

$$p_{Torr} = \frac{Nk_BT}{133.323}. \tag{4}$$

According to Equations (3) and (4), the number density of alkali metals can be calculated by:

$$N = \frac{1}{T}10^{32.178-4040/T}. \tag{5}$$

Figure 1 clearly shows the relationship between the Rb saturated vapor pressure and temperature, and the relationship between the Rb number density and temperature.

2.2. Spectral Absorption Theory

When a parallel laser beam near the alkali metal D-line vertically passes through the alkali metal vapor cell, the intensity of the transmitted laser beam will be attenuated: $I_{\text{out}} = I_{in}\exp[-N\sigma(\nu)l]$. In the case of high buffer-gas pressure, the absorption cross-section can be approximated by the Lorentzian profile, $\sigma(\nu) = \pi r_e c f \cdot \mathcal{L}(\nu)$.

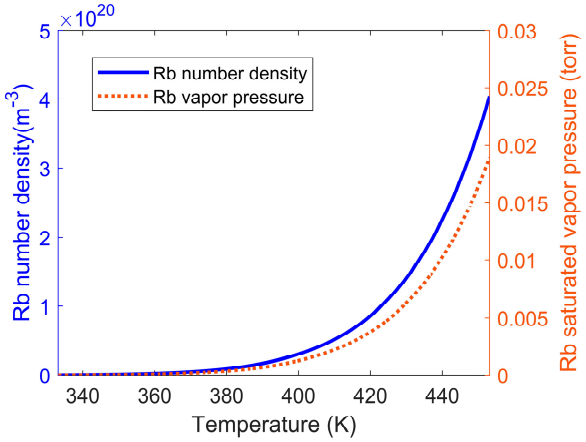

Figure 1. Rb saturated vapor pressure and Rb number density at different temperatures, as calculated from Equations (3) and (5).

Since Walkup et al. [24] found that in the near wings, asymmetry occurs because the used linear relationship is not suitable for the impact approximation, the Lorentzian profile thus needs to be modified as:

$$\mathcal{F}(\nu) = \frac{\Gamma}{2\pi} \frac{1 + 0.6642 \times 2\pi T_d \Delta}{[\Delta^2 + (\Gamma/2)^2]}, \tag{6}$$

where T_d is the collision duration.

Since the D1 line of ^{87}Rb consists of four transitions, as shown in Figure 2, the absorption cross-section becomes:

$$\sigma(\nu) = \sum_{F_g \to F_e} A_{F_g \to F_e} \sigma(\nu - \nu_{F_g \to F_e}). \tag{7}$$

where $A_{F_g \to F_e}$ is shown in Table 1.

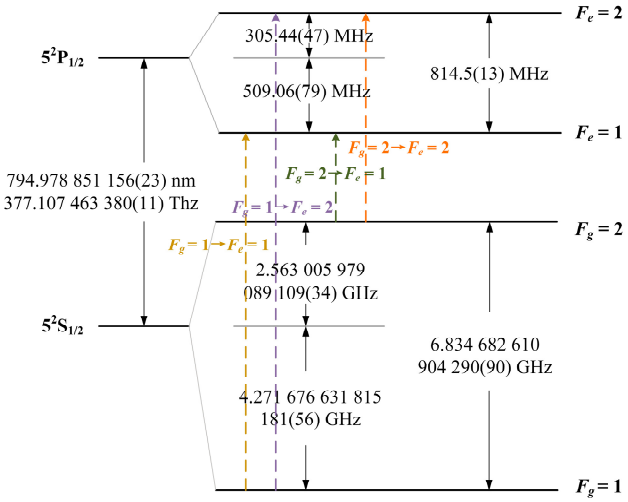

Figure 2. The schematic of the ^{87}Rb transitions between the hyperfine levels of the ground and excited states of the D1 transitions.

Table 1. Relative strengths $A_{F_g \to F_e}$ of the individual D1 hyperfine resonances for photon absorption.

Transition	$A_{F_g \to F_e}$
Fg = 1→Fe = 1	1/16
Fg = 1→Fe = 2	5/16
Fg = 2→Fe = 1	5/16
Fg = 2→Fe = 2	5/16

According to Equations (6) and (7), the ratio of the transmitted beam intensity and the incident beam intensity can be obtained by:

$$-\ln \frac{I_{out}}{I_{in}} = N\pi r_e cfl \sum_{F_g \to F_e} A_{F_g \to F_e} \frac{\Gamma}{2\pi} \frac{1 + 0.6642 \times 2\pi T_d \Delta'}{[\Delta'^2 + (\Gamma/2)^2]}, \quad (8)$$

where $\Delta' = \nu - \nu_{F_g \to F_e} - \delta$.

The density of alkali metals can be obtained according to Equation (12).

3. Device Design and Experimental Setup

3.1. Device Design

In order to realize the direct and effective measurement of the internal temperature of the cell, the design method of this paper is to seal the platinum temperature sensor (PT1000) into the glass cell and design the cell as a double stem. The schematic of the temperature-measuring device design is shown in Figure 3.

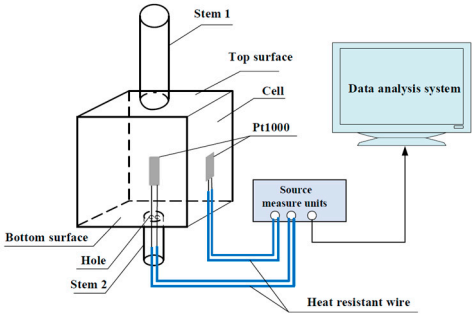

Figure 3. Schematic of the temperature-measuring device design.

Stem 1 is connected to the top surface of the cell as a path for situating the platinum temperature sensor in the cell, while Stem 2 is connected to the bottom surface of the cell. It should be noted that the through-holes between Stem 2 and the bottom wall are not completely open. There are only two through-holes, with a diameter of 1 mm and a spacing of 2 mm, which are used to position the two pins of the platinum temperature sensor. The two through-holes are designed to prevent the short circuit that would be caused by the contact of the platinum temperature sensor pins.

The platinum temperature sensor, which measures the outer wall temperature of the cell, can be pasted onto the glass wall using a thermal conductive adhesive. Source-measure units can collect the voltage signal generated by the platinum temperature sensor, which is processed by the data analysis system to obtain the temperature value.

This section has been divided using subheadings. It should provide a concise and precise description of the experimental results and their interpretation, as well as the experimental conclusions that can be drawn.

3.2. Device Fabrication

The cell designed in Section 3.1 is shown in Figure 4a. The material of the cell is made of Pyrex, the side length of the cube cell is 15 mm, the wall thickness is 1 mm, and the inner

diameter of the stem is 4 mm. After the platinum temperature sensor is encapsulated in the cell, we connect stem1 to the inflation pipeline, and charge the cell with ^{87}Rb and 700 torr N_2 at room temperature (25 °C). The filled cell is shown in Figure 4b.

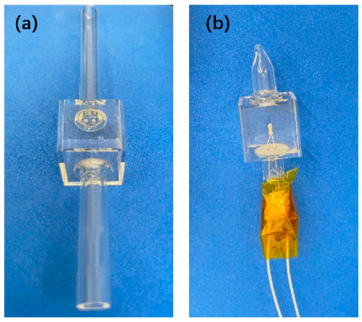

Figure 4. Temperature-measuring device. (**a**) The structure of cell. (**b**) Sealed cell, with ^{87}Rb and 700 torr N_2.

During the manufacturing process, it should be noted that when we tried to seal the two pins of the platinum temperature sensor with the Pyrex stem, it was found that the vacuum degree of the seal was not good enough (leak detector > 1×10^{-8} Pa·m^3/s). The reason for this phenomenon is that the thermal expansion coefficients of Pyrex glass and the platinum temperature sensor pins are different. The thermal expansion coefficients of Pyrex glass, Dumet, Kovar alloy, and platinum are 3.3×10^{-6} K^{-1}, 8×10^{-6} K^{-1}, 5×10^{-6} K^{-1}, and 9×10^{-6} K^{-1}, respectively.

We tried Dumet wire, Kovar alloy, and platinum wire successively; the results show that there is a gap between the sealed Pyrex glass and the three metal pins, which can be clearly observed through an electronic magnifying glass, as shown in Figure 5.

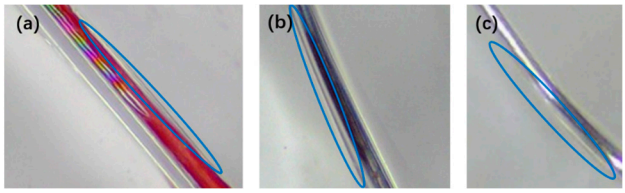

Figure 5. The sealing conditions of Pyrex glass and the different kinds of metal wires. The gap between Pyrex glass and the metal is marked by blue ellipses. (**a**) Dumet wire. (**b**) Kovar alloy. (**c**) Platinum wire.

In order to solve this problem and consider the production cost, we chose an epoxy resin adhesive to seal the gap. The epoxy resin adhesive has the advantages of good insulation, high sealing performance, and high temperature resistance. After being sealed with epoxy resin adhesive, the cell could meet the requirements of sealing vacuum degree at room temperature and high temperature (60 °C~200 °C) (leak detector < 1×10^{-10} Pa·m^3/s).

3.3. Experimental Setup

The experimental setup is shown in Figure 6, in which the cell created in Section 3.2 is placed in an electric wire oven and then heated by thermal radiation. The probe laser is a distributed-feedback (DFB) laser with a center wavelength of 795 nm. The wavelength of the probe beam is measured in real time, using a wavelength meter (Highfinesse WS7, Germany). In the experiment, the combination of a half-wave plate and a polarization beam splitter (PBS) is used to adjust the light intensity of the beam, to ensure the linear polarization of the beam. A non-polarizing cube beam splitter (NPBS) is used to divide the linearly polarized beam into two beams with equal light intensity, one of which is received by the photodetector 1 and the other enters the oven. The probe beam can enter the cell

through the optical aperture on the wall of the oven and enter from the center of the cell. At the same time, it is necessary to avoid platinum resistance to prevent it from blocking the detection light. Since the light intensity used to measure the density of ^{87}Rb is weak (< 1 uw), the measurement system needs to use an optical chopper (Thorlabs mc2000b, photo mc2f330, America) to modulate the probe beam; the modulation frequency here is 350 Hz. After that, the output signal of the photodetector is demodulated by the lock in the amplifier. Finally, the output signal of the temperature sensor is collected by the host computer and demodulated by the phase-locked amplifier.

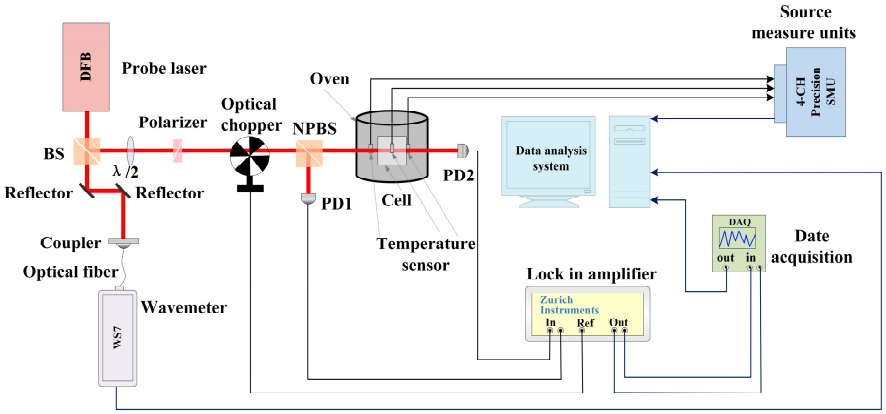

Figure 6. Schematic of the Rb vapor-density measurement system.

4. Results and Discussion

The three PT1000 are used to measure the internal temperature of the cell, the external wall temperature of the cell, and the air temperature in the oven, respectively, as shown in Figure 6. The temperature measurement results are shown in Figure 7, in which the early oscillation is caused by the temperature control of the oven itself (this part is not included in the current paper as a key analysis content). The experiment showed that when the temperature difference between the outer wall of the cell and the inner wall of the cell tends to be stable, the average temperature difference is 0.39 K, and the standard deviation is 0.04 K. After the internal temperature of the cell has become stable, the fluctuation range of the internal temperature of the cell is within $\pm$ 0.1 K. Since there is a temperature difference between the inner and outer walls of the measured cell, the temperature used in the spectral absorption experiment is the temperature value fed back by the PT1000 inside the cell.

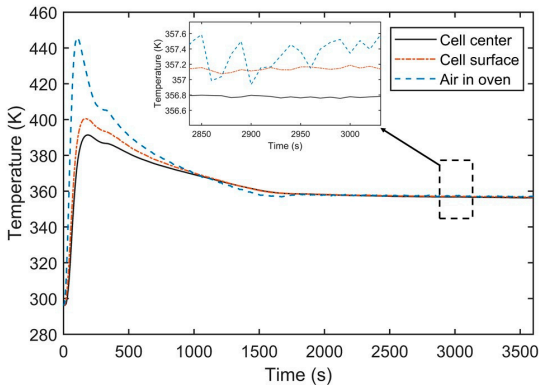

Figure 7. Experimental results at various temperatures. The temperature of the cell center is plotted as a solid line, the temperature of the cell surface is plotted as a dash–dotted line, and the temperature of the oven is plotted as a dotted line.

The experiment was carried out at ten different temperatures, in which the cell was in the absorption spectrum near the ^{87}Rb D1 line. During the measurement process, the light

intensity of the detection laser needs to be continuously reduced until the line shapes no longer change. The experimental results in the wavelength range of 794.925 nm~795.075 nm are shown in Figure 8, where the abscissa is the frequency of the detection beam offset D1 line. It can be seen that the height of the spectral line increases visibly with the increase in temperature.

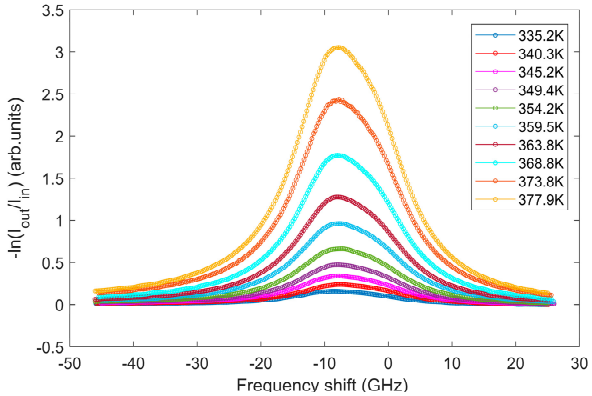

Figure 8. Experimental results of absorption spectrum for 87Rb D1 line broadened by N2 at different temperatures.

The line shape of the alkali metal absorption spectrum has been described in Section 2.2. For fitting the data, Equation (8) can be rewritten as:

$$-\ln\frac{I_{out}}{I_{in}} = a \cdot \sum_{F_g \to F_e} A_{F_g \to F_e} \frac{1 + b \cdot \Delta'}{[\Delta'^2 + (\Gamma/2)^2]}, \tag{9}$$

where the relationship between the constant, a, and the density of the alkali metals, N, is shown below:

$$a = N r_e c f l \Gamma / 2. \tag{10}$$

By fitting the experimental results in Figure 7 with Equation (9), the fitting coefficient, a, and the line width (FWHM) for calculating the ^{87}Rb density can be obtained. Figure 9 shows the experimental data, measured at 368.8 K, and the fitting results.

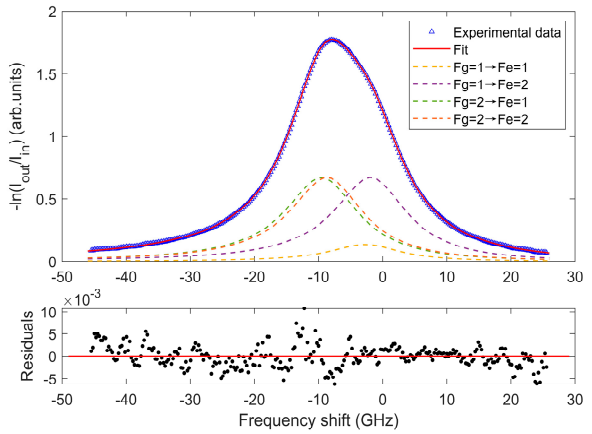

Figure 9. Fitting profile of the experimental results (368.8 K). The ^{87}Rb transitions between hyperfine levels of the ground and excited states of the D1 transitions are plotted as dotted lines.

By substituting the fitting coefficient, a, and line width (FWHM) under different temperatures into Equation (10), the density of ^{87}Rb at the corresponding temperature can be obtained. The comparison between the ^{87}Rb density, as measured by the absorption spectrum, and the ^{87}Rb density (Equation (5)) derived from the empirical formula, Equation (1),

for the saturated vapor pressure is shown in Figure 6. It can be seen that the growth trend of the absorption spectrum's experimental results is consistent with the empirical formula of saturated vapor pressure, but the experimental results are smaller than the calculation results of Equation (5).

In this study, the internal temperature measurement device of the cell is designed and manufactured to reduce the error caused by the inaccuracy of temperature measurement. After excluding the influence of temperature, the cells used in the previous experiments, where the measured density is lower than the empirical formula of saturated vapor pressure, are all made from Pyrex, so the low density of ^{87}Rb measured in the experiment may be due to the penetration of alkali metal and Pyrex glass and other polluting reactions during the process of filling the cells.

If the measurement results in this paper are used to fit the empirical density formula (context logic) specific to the Pyrex glass cell, and if it is assumed that the density formula of ^{87}Rb vapor suitable for the Pyrex glass cell is only different from the empirical formula of saturated vapor pressure by coefficients a and B, then the density formula obtained by fitting the experimental data is:

$$N = \frac{1}{T} 10^{31.992 - 3991/T}. \tag{11}$$

The fitting results are shown in Figure 10, and the uncertainty of fitting is only 4%.

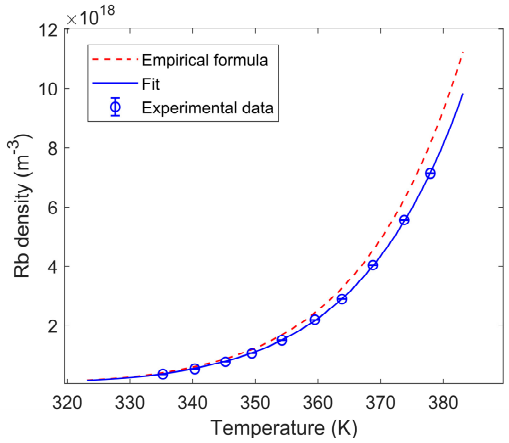

Figure 10. Comparison of experimental results of Spectral absorption and empirical formula calculation.

In addition to the measurement of the density of ^{87}Rb, the dependence of pressure spreading and the frequency shift of spectral lines on temperature are also studied with this experimental system. When the applied potentials of the upper and lower levels of the emitting atom are approximated by a simple inverse law, the temperature variations in the line widths of the pressure-broadened spectral lines can be represented by a power–law relationship [25]:

$$\gamma = C \cdot T^n, \tag{12}$$

where γ is the pressure broadening coefficient, and C and n are the parameters.

Figures 11 and 12 show the fitting results of the relationship between the measured line widths, as well as the frequency shifts and the temperature, in which the fitting formulas that are used are as follows:

$$\frac{\Gamma_{T_1}}{\Gamma_{T_2}} = \left(\frac{T_1}{T_2}\right)^n + \alpha, \tag{13}$$

$$\frac{\delta_{T_1}}{\delta_{T_2}} = \left(\frac{T_1}{T_2}\right)^{n'} + \beta, \tag{14}$$

where T_2 = 368.8 K. The coefficients from the fits are presented in Table 2. The parameters α and β are generally consistent with 0, which conforms to Equation (12).

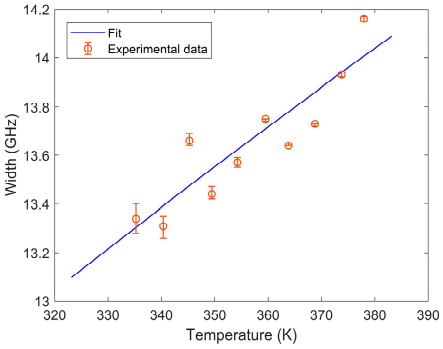

Figure 11. The measured line widths for ^{87}Rb (D1) as a function of temperature for N_2 (700 Torr at 25°C) with linear fits from Equation (13).

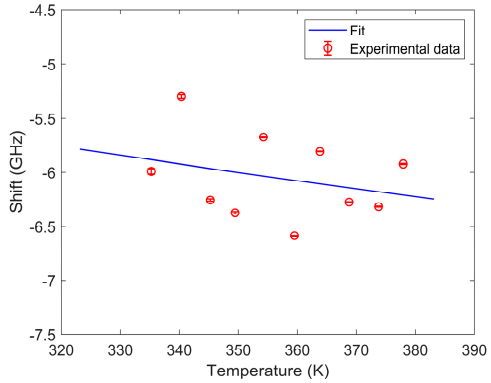

Figure 12. Measured shifts for ^{87}Rb (D1) as a function of temperature for N_2 (700 Torr at 25°C) with linear fits derived from Equation (14).

Table 2. The fits to the measured line widths and frequency shifts of N_2, as a function of temperature.

	n/n'	α/β (GHz)
^{87}Rb D1 Width	0.43 (±0.17)	0.11 (±0.11)
^{87}Rb D1 Shift	0.44 (±1.22)	0.13 (±0.38)

5. Conclusions

In this paper, a device is presented that can directly measure the internal temperature of an alkali metal cell and that has been designed for the first time. The designed device can ensure that the vacuum degree reaches 5.6 × 10^{-11} Pa·m^3/s of tightness and the temperature sensor does not react with alkali metal, which can ensure the reliability of measurement. Due to the advantages of a simple production method, low cost, and high reliability, the designed device can be used to measure the internal temperature of various types of cells, to help evaluate the performance of the heating system.

The absorption spectrum line of ^{87}Rb D1 with 700torr N_2 was measured and the absorption spectrum line was fitted by combining the pressure-broadening model with the transition process of four hyperfine levels so that a good fitting effect was obtained.

The ^{87}Rb vapor density at different temperatures in the Pyrex cell was measured using the designed device. The relationship between ^{87}Rb vapor density and temperature was analyzed, and the corresponding calculation formula with an uncertainty of only 4% is given. At the same time, the temperature dependence index of the line widths and line shifts were also measured.

Author Contributions: Conceptualization, H.S. and S.Z.; methodology, H.S.; validation, H.S., S.Z., W.Z. and F.Z.; formal analysis, H.S.; investigation, H.S. and S.Z.; data curation, H.S.; writing—original draft preparation, H.S.; writing—review and editing, S.Z. and S.L.; project administration, W.Q., S.Z. and B.Z.; funding acquisition, W.Q. All authors have read and agreed to the published version of the manuscript.

Funding: This work was supported by grants from the National Science Fund for the Distinguished Young Scholars of China, No. 61925301, the Beijing Natural Science Foundation, No. 1222025, the National Natural Science Foundation of China (NSFC), Nos. 62003022 and 61627806, the National Key Research and Development Program of China, No. 2018YFB2002405.

Institutional Review Board Statement: Not applicable.

Informed Consent Statement: Not applicable.

Data Availability Statement: The data presented in this study are available on reasonable request from the corresponding author.

Conflicts of Interest: The authors declare no conflict of interest.

References

1. Tang, J.; Liu, Y.; Wang, Y.; Zhou, B.; Han, B.; Zhai, Y.; Liu, G. Enhancement of bandwidth in spin-exchange relaxation-free (SERF) magnetometers with amplitude-modulated light. *Appl. Phys. Lett.* **2022**, *120*, 084001. [CrossRef]
2. Yan, Y.; Lu, J.; Zhou, B.; Wang, K.; Liu, Z.; Li, X.; Wang, W.; Liu, G. Analysis and correction of the crosstalk effect in a three-axis SERF atomic magnetometer. *Photonics* **2022**, *9*, 654. [CrossRef]
3. Lu, F.; Wang, S.; Xu, N.; Li, B.; Lu, J.; Han, B. Analysis and suppression of the cross-axis coupling effect for dual-beam serf atomic magnetometer. *Photonics* **2022**, *9*, 792. [CrossRef]
4. Zou, S.; Morin, D.J.; Weaver, C.; Armanfard, Z.; Muschell, J.; Nahlawi, A.I.; Saam, B. Collisional electron paramagnetic resonance frequency shifts in Cs-Rb-Xe mixtures. *Phys. Rev. A* **2022**, *106*, 012801. [CrossRef]
5. Gentile, T.R.; Nacher, P.J.; Saam, B.; Walker, T.G. Optically polarized ^{3}He. *Rev. Mod. Mod. Phys.* **2017**, *89*, 045004. [CrossRef] [PubMed]
6. Driehuys, B.; Cates, G.D.; Miron, E.; Sauer, K.; Walter, D.K.; Happer, W. High-volume production of laser-polarized 129Xe. *Appl. Phys. Lett.* **1996**, *69*, 1668. [CrossRef]
7. Ruset, I.C.; Ketel, S.; Hersman, F.W. Optical Pumping System Design for Large Production of Hyperpolarized 129Xe. *Phys. Rev. Lett.* **2006**, *96*, 053002. [CrossRef]
8. Norquay, G.; Collier, G.J.; Rao, M.; Stewart, N.J.; Wild, J.M. 129Xe-Rb Spin-Exchange Optical Pumping with High Photon Efficiency. *Phys. Rev. Lett.* **2018**, *121*, 153201. [CrossRef]
9. Killian, T.J. Thermionic phenomena caused by vapors of rubidium and potassium. *Phys. Rev.* **1926**, *27*, 578–587. [CrossRef]
10. Alcock, C.B.; Itkin, V.P.; Horrigan, M.K. Vapour pressure equations for the metallic elements: 298–2500 K. *Can. Metall. Q.* **1984**, *23*, 309–313. [CrossRef]
11. Cohen, R.D.; Mullarkey, C.A.; Howell, J.C.; Katz, N. Polarization-independent atomic prism filter for removing amplified spontaneous emission. *Appl. Opt.* **2018**, *57*, 4472–4476. [CrossRef] [PubMed]
12. Tang, Y.; Wen, Y.; Cai, L.; Zhao, K.F. Spin-noise spectrum of hot vapor atoms in an anti-relaxation-coated cell. *Phys. Rev. A* **2020**, *101*, 013821. [CrossRef]
13. Kawano, H. Effective Work Functions of the Elements: Database, Most probable value, Previously recommended value, Polycrystalline thermionic contrast, Change at critical temperature, Anisotropic dependence sequence, Particle size dependence. *Prog. Surf. Sci.* **2021**, *97*, 100583.
14. Kelley, M.; Burant, A.; Branca, R.T. Resolving the discrepancy between theoretical and experimental polarization of hyperpolarized 129Xe using numerical simulations and in situ optical spectroscopy. *J. Appl. Phys.* **2020**, *128*, 144901. [CrossRef]
15. Seltzer, S.J. Developments in Alkali-Metal Atomic Magnetometry. Ph.D. Thesis, Dept. Physics, Princeton University, Princeton, NJ, USA, 2008.
16. Smullin, S.J.; Savukov, I.M.; Vasilakis, G.; Ghosh, R.K.; Romalis, M.V. Low-Noise High-Density Alkali Metal Scalar Magnetometer. *Phys. Rev. A* **2009**, *80*, 033420. [CrossRef]
17. Schrank, G. Characterization of a low-pressure high-capacity 129Xe flow-through polarizer. *Phys. Rev. A* **2002**, *80*, 063424. [CrossRef]
18. Jau, Y.Y.; Kuzma, N.N.; Happer, W. High-field measurement of the 129Xe-Rb spin-exchange rate due to binary collisions. *Phys. Rev. A* **2002**, *66*, 052710. [CrossRef]
19. Chann, B.; Babcock, E.; Anderson, L.W.; Walker, T.G. Measurements of 3He spin-exchange rates. *Phys. Rev. A* **2002**, *66*, 032703. [CrossRef]
20. Savukov, I.M.; Romalis, M.V. Effects of spin-exchange collisions in a high-density alkali-metal vapor in low magnetic fields. *Phys. Rev. A* **2005**, *71*, 023405. [CrossRef]

21. Lu, J.X.; Wang, J.; Yang, K.; Zhao, J.P.; Quan, W.; Han, B.C.; Ding, M. In-Situ Measurement of Electrical-Heating-Induced Magnetic Field for an Atomic Magnetometer. *Sensors* **2020**, *20*, 1826. [CrossRef]
22. Nikolaou, P.; Coffey, A.M.; Ranta, K.; Walkup, L.L.; Gust, B.M.; Barlow, M.J.; Rosen, M.S.; Goodson, B.M.; Chekmenev, E.Y. Multidimensional Mapping of Spin-Exchange Optical Pumping in Clinical-Scale Batch-Mode 129Xe Hyperpolarizers. *J. Phys. Chem. B* **2014**, *118*, 4809–4816. [CrossRef] [PubMed]
23. Kornack, T.W. A Test of CPT and Lorentz Symmetry Using a K-3He Co-Magnetometer. Ph.D. Thesis, Dept. Physics, Princeton University, Princeton, NJ, USA, 2005.
24. Walkup, R.; Stewart, B.; Pritchard, D.E. Collisional line broadening due to van der Waals potentials. *Phys. Rev. A* **1984**, *29*, 169. [CrossRef]
25. Helmi, M.S.; Roston, G.D. Power-law dependence of pressure broadening of spectral lines on temperature. *AIP Conf. Proc.* **2001**, *559*, 347–350.